

UC Davis

UC Davis Previously Published Works

Title

Magnetism and Thermoelectric Properties of the Zintl Semiconductor: Eu₂₁Zn₄As₁₈.

Permalink

<https://escholarship.org/uc/item/6x73z0zj>

Journal

Chemistry of Materials, 36(23)

ISSN

0897-4756

Authors

Islam, Md

Wróblewska, Maria

Shen, Zihao

et al.

Publication Date

2024-12-10

DOI

10.1021/acs.chemmater.4c02200

Peer reviewed

Magnetism and Thermoelectric Properties of the Zintl Semiconductor: $\text{Eu}_{21}\text{Zn}_4\text{As}_{18}$

Published as part of *Chemistry of Materials* special issue “In Memory of Prof. Francis DiSalvo”.

Md. Minhajul Islam, Maria Wróblewska, Zihao Shen, Eric S. Toberer, Valentin Taufour, and Susan M. Kauzlarich*



Cite This: *Chem. Mater.* 2024, 36, 11499–11508



Read Online

ACCESS |



Metrics & More

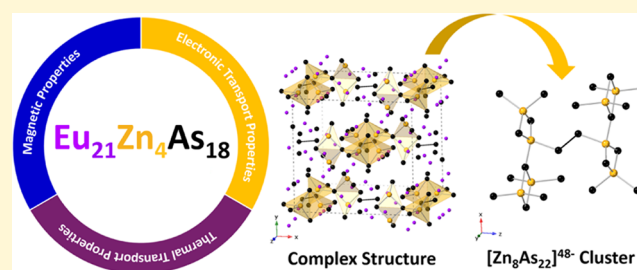


Article Recommendations



Supporting Information

ABSTRACT: Compositional diversity and intriguing structural features have made Zintl phases excellent candidates as thermoelectric materials. Zintl phase with 21-4-18 composition has shown high thermoelectric performance in the mid- to high-temperature ranges. The complex crystal structure and favorable transport properties of these compounds indicate the potential for high thermoelectric efficiency. Arsenic-based $\text{Eu}_{21}\text{Zn}_4\text{As}_{18}$, belonging to the $\text{Ca}_{21}\text{Mn}_4\text{Sb}_{18}$ structure type, exhibits a semiconductor-like p-type transport behavior and has a calculated band gap of 0.49 eV. The compound is paramagnetic at high temperatures, with an antiferromagnetic transition occurring at $T_N = \sim 10$ K. The moment obtained from the Curie–Weiss data fit aligns with Eu^{2+} ions. At the same time, the field-dependent measurement at 2 K indicates complex magnetic ordering with a saturation moment consistent with Eu^{2+} ions. Pristine $\text{Eu}_{21}\text{Zn}_4\text{As}_{18}$ exhibits an ultralow lattice thermal conductivity of $0.40 \text{ W m}^{-1} \text{ K}^{-1}$ at 873 K. Electronic transport properties measurement shows evidence of bipolar conduction across much of the measured temperature range (450–780 K). However, the Seebeck coefficient remains extremely high ($>440 \mu\text{V K}^{-1}$) across this range, indicating the potential for high zT if an appropriate dopant is found. This work represents the first report on the temperature-dependent thermal conductivity, Seebeck coefficient, and thermoelectric efficiency of the arsenic-containing Zintl phase with 21-4-18 composition, showcasing its promise for further optimization of the thermoelectric performance.



1. INTRODUCTION

Thermoelectricity holds the promise of being an ecofriendly solution for generating clean energy from waste heat. This niche technology can complement popular clean energy sources, such as solar, wind, and geothermal sources, to enhance energy generation and distribution efficiency. Moreover, thermoelectric materials can also be used in other heat-generating applications, including heavy industries and electric vehicles, to improve energy utilization and reduce operational energy loss. The efficiency of thermoelectric materials is calculated by the dimensionless figure of merit, $zT = S^2T/\rho\kappa$, where S is the Seebeck coefficient, T is the absolute temperature, ρ is the electrical resistivity, and κ is the total thermal conductivity ($\kappa = \kappa_l + \kappa_e$, where κ_l is the lattice thermal conductivity and κ_e is the electronic thermal conductivity).¹ One approach to improve zT entails reducing the lattice thermal conductivity by deploying strategies, such as grain-boundary engineering through microstructural modification,² hierarchical architectures,³ and introducing nanoprecipitates.⁴ Another method for enhancing zT is by improving the electronic properties through carrier concentration tuning,⁵ band convergence,¹ and band sharpening.⁶ However, the

thermoelectric properties are complexly interrelated, making optimization of the thermoelectric properties to provide an overall high zT a difficult task.

Zintl phases have become excellent candidates for thermoelectric applications due to possessing high mobility regions like electron-crystal and phonon-inhibiting regions like phonon-glass.⁷ However, despite possessing unique bonding and properties compared to the heavier pnictides, such as antimony and bismuth,^{8,9} arsenic-containing Zintl phases have only recently drawn interest for thermoelectric applications.^{10–12} Arsenic-containing Zintl phases have also been highlighted for other properties, such as topological insulators,¹³ superconductors,^{14,15} and magnetism.¹⁶ Due to the complexities of tuning properties, materials with inherently low lattice thermal conductivity have become attractive choices

Received: August 5, 2024

Revised: November 12, 2024

Accepted: November 13, 2024

Published: November 22, 2024



for exploring thermoelectric properties.¹⁷ Zintl phases, such as $\text{Yb}_{14}\text{MnSb}_{11}$,¹⁸ $\text{Yb}_{10.5}\text{MgSb}_9$,¹⁹ and $\text{Yb}_{21}\text{Mn}_4\text{Sb}_{18}$,²⁰ possess large complex crystal structures leading to intrinsically low lattice thermal conductivity. The lattice thermal conductivity is derived from the equation $\kappa_{\text{lattice}} = 1/3 C_v \nu_g l$, where C_v is the specific heat capacity, ν_g is the phonon group velocity, and l is the phonon mean free path.²¹ High density in Zintl phases leads to minimum variations in the heat capacity regardless of the composition.²² As a result, the phonon group velocity and phonon mean free path act as dominating factors in determining the lattice thermal conductivity. Zintl compounds have a low phonon group velocity due to the presence of heavy atoms and soft covalent bonding in their structural units. This is further influenced by the large crystal structures with many atoms and flattened phonon modes, which result from increased gaps between phonon modes caused by the large mass contrast. On the other hand, the phonon mean free path is determined by the scattering mechanisms such as phonon–phonon scattering, point defect scattering, and boundary scattering. The presence of anharmonic bonds and rattling atoms leads to increased scattering of phonons. Overall, a larger volume with more atoms in the primitive cell might be conducive to low lattice thermal conductivity.¹⁷ As a result, Zintl phases with composition $\text{A}_2\text{M}_4\text{Pn}_{18}$ ($\text{A} = \text{Ca}, \text{Sr}, \text{Ba}, \text{Eu}, \text{Yb}$; $\text{M} = \text{Mn}, \text{Zn}, \text{Cd}$; and $\text{Pn} = \text{As}, \text{Sb}, \text{Bi}$) could potentially exhibit ultralow lattice thermal conductivity because of possessing volume $>4000 \text{ \AA}^3$ and >300 atoms per unit cell.^{23,24}

Zintl phases with the composition $\text{A}_2\text{M}_4\text{Pn}_{18}$ have unique structural features suitable for thermoelectric applications.^{23–25} There are subtle differences that arise from the connectivity of the MPn_4 structural units, leading to different structure types within this class of compounds. The compounds of this composition crystallize in different space groups: $C2/c$, $C2/m$, and $Cmce$. $\text{Eu}_{21}\text{Zn}_4\text{As}_{18}$ contains a large unit cell boasting 84 Eu^{2+} cations, 6 $[\text{As}_2]^{4-}$ dumbbells, 16 isolated As^{3-} anions, and 2 $[\text{Zn}_8\text{As}_{22}]^{48-}$ clusters formed by connecting edges and corners of $[\text{ZnAs}_4]$ tetrahedral subunits.²⁴ Its large and complex crystal structure might help attain a low lattice thermal conductivity, while a high density of states (DOS) near the Fermi level could result in a high Seebeck coefficient for this composition.²⁶ Though structural and magnetic properties of different compounds of this composition have been reported in the literature, only $\text{Yb}_{21}\text{Mn}_4\text{Sb}_{18}$ has been investigated for thermoelectric efficiency.^{20,26} $\text{Yb}_{21}\text{Mn}_4\text{Sb}_{18}$ (band gap 0.394 eV) shows impressive thermoelectric performance at medium-high temperatures, reaching a peak zT of 0.8 at 800 K. However, bipolar conduction is observed above 600 K in this compound. Having the more electro-negative arsenic atom in the anionic unit leads to a higher band gap in compounds with similar compositions and, therefore, should suppress carrier excitations and reduce the impact of bipolar transport on the Seebeck coefficient at high temperatures.¹⁸ This suggests that arsenic-based $\text{Eu}_{21}\text{Zn}_4\text{As}_{18}$ might also be a good thermoelectric material.

In this work, high-purity polycrystalline $\text{Eu}_{21}\text{Zn}_4\text{As}_{18}$ (21-4-18) samples were prepared via ball-milling, using binary precursors and subsequent high-temperature annealing. In the investigation of the synthetic route, progressive growth in the crystallinity of the samples was observed by systematically increasing the annealing temperature. The phase purity was determined using powder X-ray diffraction (PXRD) analysis and Rietveld refinement, while energy dispersive spectroscopy (EDS) confirmed the homogeneous distribution of elements in

the compound. We have explored the incorporation of Na^+ (1.02 \AA)/ K^+ (1.38 \AA) as dopants into the Eu^{2+} (1.17 \AA) sites to optimize the thermoelectric properties. Temperature and field-dependent magnetization studies show that Eu is Eu^{2+} with a Curie–Weiss temperature dependence and an antiferromagnetic transition at about 10 K. The saturation moment at 2 K with an applied 7 T field confirms the Eu^{2+} oxidation state. Laser flash analysis (LFA) confirms that $\text{Eu}_{21}\text{Zn}_4\text{As}_{18}$ possesses ultralow lattice thermal conductivity, as anticipated, which is a good starting point for optimizing thermoelectric properties through carrier concentration modification. Moreover, electrical resistivity and Hall measurements revealed insights into the electrical transport properties of the compound. Finally, the Seebeck coefficient is reported for the thermoelectric efficiency of arsenic-based 21-4-18 for the first time, showing the promise of this phase for thermoelectric applications.

2. EXPERIMENTAL SECTION

2.1. Reagents. Eu Ingot (Stanford Advanced Materials, 99.99%), Zn shots (Alfa Aesar, 99.999%), As chips (Johnson Matthey Chemicals, 99.9999%), NaH (Sigma-Aldrich, 95%), and KH (Sigma-Aldrich, 30 wt % dispersion in mineral oil) were used for the synthesis. KH was washed with hexane several times to remove the oil and was dried under a dynamic vacuum overnight. All elements and reagents were handled inside an argon-filled glovebox with an oxygen level <0.5 ppm. Binary precursor EuAs was synthesized by taking the elements in a 1:1 ratio in a stainless-steel ball mill vial. The vial was sealed in a Mylar bag and milled for 30 min in a mixer machine. After the first milling, the wall of the vial was scrapped with a chisel inside the glovebox. The powder was milled again for 1 h by flipping the vial after 30 min. The sample was annealed at $850 \text{ }^\circ\text{C}$ using a ramp rate of $100 \text{ }^\circ\text{C h}^{-1}$ for 12 h. Zn_3As_2 was also synthesized by adding stoichiometric amounts of the elements to a ball mill vial and following the same procedure as described above for EuAs but annealing at $650 \text{ }^\circ\text{C}$ with a ramp rate of $100 \text{ }^\circ\text{C h}^{-1}$ for 12 h. The powder X-ray diffraction (PXRD) patterns are provided in the Supporting Information (SI), Figures S1 and S2.

Caution: NaH and KH are highly reactive to moisture. They must be handled carefully under an inert atmosphere or inside a glovebox.

2.2. Synthesis. Powder samples of $\text{Eu}_{21}\text{Zn}_4\text{As}_{18}$ were prepared using binary precursors following an adaptation of our group's previous works.^{26,27} Stoichiometric amounts of EuAs, Zn_3As_2 , and Eu metal were added to a stainless-steel ball mill vial with a Viton O-ring. The vial was sealed inside a Mylar bag to ensure that no oxidation occurred during milling. The reagents were mechanically milled in a SPEX8000 M high-energy ball mill mixer machine for 30 min. The vial was then scraped with a chisel inside the glovebox and milled again for 1 h (the vial was flipped after 30 min). The homogeneously mixed powder was loaded into a one-side welded Ta tube inside the glovebox, and the open end was crimped shut. The Ta tube was transferred under $\text{Ar}(\text{g})$ to an $\text{Ar}(\text{g})$ arc welder to seal the other side. The sealed Ta tube was encapsulated inside a quartz tube under a vacuum. The reagents were heated at 650, 800, and $950 \text{ }^\circ\text{C}$ using a ramp rate of $100 \text{ }^\circ\text{C h}^{-1}$ for 96 h.

The doped samples of $\text{Eu}_{21-x}\text{Na}_x\text{Zn}_4\text{As}_{18}$ were synthesized by taking the molar ratio of the elements as $\text{Eu}/\text{Na}/\text{Zn}/\text{As} = 21 - x : x : 4:18$ ($x = 0.1$ and 0.2), where Eu, Zn, As, and Na were supplied by EuAs, Zn_3As_2 , and NaH binaries. Similarly, $\text{Eu}_{21-x}\text{K}_x\text{Zn}_4\text{As}_{18}$ ($x = 0.1$ and 0.2) samples were synthesized by using the same method described above, with the only difference being that KH was employed as the K source. The homogeneously mixed ball-milled powdered samples were heated to $950 \text{ }^\circ\text{C}$ and held for 96 h, using a ramp rate of $100 \text{ }^\circ\text{C h}^{-1}$.

Caution: The reaction of hydrides with arsenic might lead to the formation of highly toxic arsine gas. Taking the necessary precautions when handling the quartz and the metal tubes postreaction is crucial. Ball mill vials and chisels used in handling these reagents should not

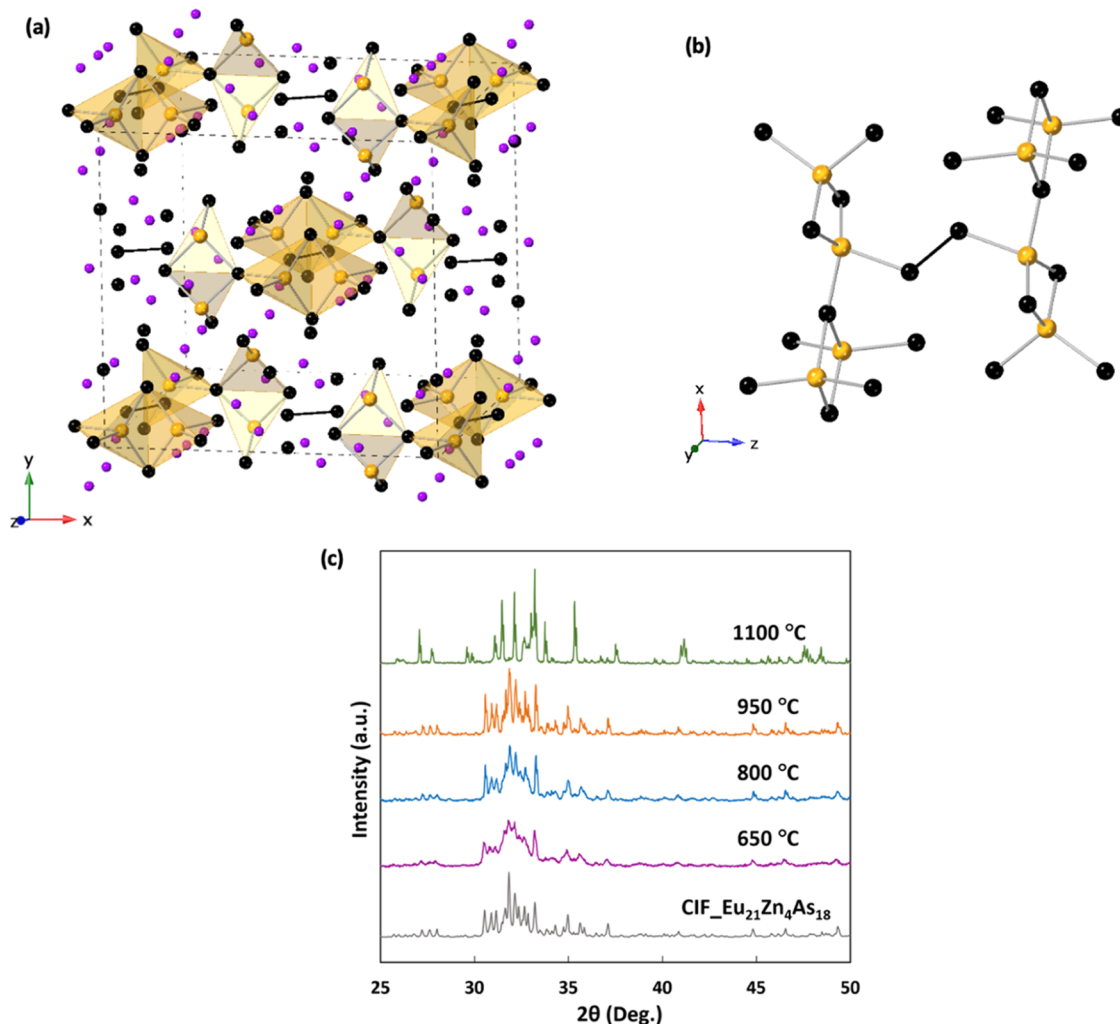


Figure 1. (a) Crystal structure of $\text{Eu}_{21}\text{Zn}_4\text{As}_{18}$ where Eu, Zn, and As are represented by purple, gold, and black spheres. The ZnAs_4 polyhedra are indicated in yellow. (b) View of the $[\text{Zn}_8\text{As}_{22}]^{48-}$ cluster in $\text{Eu}_{21}\text{Zn}_4\text{As}_{18}$. (c) Powder diffraction patterns of the reactions of $\text{Eu}_{21}\text{Zn}_4\text{As}_{18}$ at different temperatures compared with the CIF.

be immediately cleaned with water. All procedures must be conducted under a fume hood with proper personal protective equipment.

2.3. Powder X-Ray Diffraction (PXRD). The synthesized samples were ground and analyzed with a Bruker D8 ECO ADVANCE X-ray diffractometer on zero-background off-axis quartz plates. The finely ground powder was placed on quartz plates by using solvent-smearing techniques with ethanol. The scans were 80 min long, utilizing $\text{Cu K}\alpha$ radiation in the 2θ angle $20\text{--}80^\circ$ with a step size of 0.02° operated at 40 kV and 25 mA. GSAS-II²⁸ software was used to analyze the powder pattern employing Rietveld refinement.

2.4. Spark Plasma Sintering. The powder sample was ground and sieved through a 100-mesh screen before loading into a 12.7 mm graphite die. The die was carefully sealed with graphite foils on both sides of the plunger to ensure air-free conditions. The powder was initially cold pressed using a Dr. Sinter Junior Spark Plasma Sintering system (Fuji Electronic Industrial Co., LTD) under Ar gas. The powder was sintered to 850°C in 10 min while the force was gradually increased from 6 to 10.5 kN. Then, the die was heated to 900°C and dwelled at this temperature for 30 min. The geometric densities of the samples were $>98\%$ of the theoretical density measured using the Archimedes method.

2.5. Scanning Electron Microscopy (SEM) and Energy Dispersive X-ray Spectroscopy (EDS). A piece of the densified sample was mounted on an epoxy resin disk for polishing with 1000-grit sandpaper. The sample was further polished on a polishing wheel with $1\ \mu\text{m}$ colloidal diamond suspension. The sample was analyzed

for SEM/EDS with an FEI Scios DualBeam FIB/SEM instrument equipped with an Oxford Instruments X-Max 50 mm^2 Si drift detector. The accelerating voltage was 20 kV. The secondary images were collected using a 20 kV accelerating voltage and 1.6 nA beam current with an Everhart–Thornley detector.

2.6. Magnetism. DC magnetization measurement of the pressed pallet of polycrystalline $\text{Eu}_{21}\text{Zn}_4\text{As}_{18}$ sample was carried out in a Quantum Design magnetic property measurement system (MPMS) under zero-field-cooled (ZFC) and field-cooled cooling (FCC) conditions. The mass of the sample is 12.43 ± 0.01 mg, and the error of the mass is smaller than 0.1%. The sample was loaded between two plastic straws before attaching them to the sample holder rod. The measurements were performed under an applied magnetic field of up to 7 T from 2 to 300 K.

2.7. Thermal Conductivity. The thermal diffusivity of the samples was obtained using a Netzsch LFA 457 laser flash analyzer under argon atmosphere. The pressed pellets were sprayed with graphite to ensure maximum laser absorption. The total thermal conductivity was calculated using the formula $D \times \rho \times C_p$, where D is the thermal diffusivity, ρ is the density of the sample measured by the Archimedes method, and C_p is the heat capacity of the compound. C_p is approximated from the Dulong–Petit law.

2.8. Seebeck, Resistivity, and Hall Measurement. The Seebeck coefficient of the pellets was measured using a custom-built instrument under a low pressure of 300 Torr in a nitrogen atmosphere from 300 to 775 K.²⁹ Resistivity and Hall measurements were

conducted using an in-house built instrument based on van der Pauw geometry.³⁰ The Hall coefficient measurements were done with a 15–20 mA current and 1 T magnetic field. Hall carrier concentration was estimated from the equation, $n = 1/eR_H$, where e is the charge of the electron and R_H is the Hall coefficient. Hall mobility was calculated using $\mu_H = R_H/\rho$, where ρ is the electrical resistivity.

3. RESULTS AND DISCUSSION

3.1. Synthesis and Composition. Figure 1a shows the crystal structure of $\text{Eu}_{21}\text{Zn}_4\text{As}_{18}$. The complexity of the structure arises from $[\text{ZnAs}_4]^{4-}$ subunits forming $[\text{Zn}_8\text{As}_{22}]^{48-}$ clusters, which are hallmarks of compounds with the 21-4-18 composition.²⁴ The ZnAs_4 tetrahedra connects and forms two symmetrically equivalent $[\text{Zn}_2\text{As}_6]$ subunits joined together through an As–As bond, creating the clusters, as shown in Figure 1b. $\text{Eu}_{21}\text{Zn}_4\text{As}_{18}$ structure belongs to the monoclinic space group $C2/m$ of the $\text{Sr}_{21}\text{Mn}_4\text{Sb}_{18}$ structure type, which is isostructural to a related compound $\beta\text{-Ca}_{21}\text{Mn}_4\text{Sb}_{18}$.³¹ It should be noted that there are two polymorphs (α - and β -), with $\alpha\text{-Ca}_{21}\text{Mn}_4\text{Sb}_{18}$ belonging to the $C2/c$ space group.²⁵ Our group has shown that the synthesis of complex ternary Zintl phases can be controlled by employing binary phases as reaction precursors.²⁷ A series of stoichiometric reactions with the ratio (Eu/Zn/As = 21:4:18) was carried out at different temperatures to determine the optimum temperature for phase pure synthesis of the compound. The PXRD patterns of the samples from reactions at different temperatures, along with the calculated pattern from the crystallographic information file (CIF), are shown in Figure 1c.²⁴ The samples become progressively more crystalline with increasing temperatures from 650 to 950 °C. The formation of the crystalline $\text{Eu}_{21}\text{Zn}_4\text{As}_{18}$ phase requires high temperature due to the slow solid-state diffusion, which limits the reaction rates. Increasing the temperature increases diffusion rates as it is an activated process.³² However, the diffraction peaks of the $\text{Eu}_{21}\text{Zn}_4\text{As}_{18}$ phase disappear at 1100 °C, and the more thermodynamically stable phase of $\text{Eu}_{14}\text{ZnAs}_{11}$ is observed. The comparison of the experimental data with $\text{Eu}_{14}\text{ZnAs}_{11}$ diffraction peaks is provided in SI, Figure S3.

The Rietveld refinement of PXRD data by GSAS-II software revealed acceptable agreement ($wR_p = 9.82\%$ and $\chi^2 = 1.39$) with the calculated pattern shown in Figure 2.³³ The refined lattice parameters $a = 16.9854(4)$ Å, $b = 16.1867(4)$ Å, $c = 16.7124(4)$ Å, and $\beta = 92.0249(14)$ are similar to published ones $a = 16.9580(6)$ Å, $b = 16.1660(6)$ Å, $c = 16.668(6)$ Å, and $\beta = 92.008(6)$ by Suen et al.²⁴ The theoretical density (6.95 g cm^{-3}) obtained from the refinement was close to the experimentally found value (6.87 g cm^{-3}). The crystallographic sites, fractions, multiplicity, and isotropic thermal parameters obtained from Rietveld Refinement are provided in SI, Table S1. The slight differences in lattice parameters compared to the single crystal data were due to the differences in temperature, as the PXRD was collected at room temperature while the single crystal CIF data were collected at 200 K. The Zintl formalism can be used to explain the valence-balanced nature of the compound. The structure contains 84 Eu^{2+} , 16 As^{3-} , 6 $[\text{As}_2]^{4-}$, and 2 $[\text{Zn}_8\text{As}_{22}]^{48-}$, making it charged balanced in nature.

Figure 3a,b show the PXRD patterns of samples prepared with Na and K, respectively. The patterns of $x = 0.0$, Na-doped ($x = 0.1$), and K-doped ($x = 0.1, 0.2$) samples look similar to the calculated patterns. However, Na-doped ($x = 0.2$) and K-

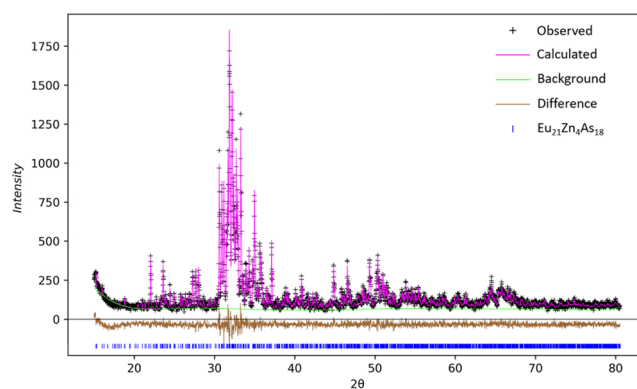


Figure 2. Rietveld refinement shows the experimental data with fit obtained from refining the structure using the crystallographic information file (CIF) from Suen et al.²⁴ The black points represent the observed data; the pink curve represents the calculated pattern from the CIF, the green line represents the background, the brown line represents the difference between the observed and calculated data, and the blue vertical lines represent the expected peaks from the crystal structure.

doped ($x = 0.3$) samples show new peaks at 31 and 34° 2θ , suggesting that Na content ($x = 0.1$) and K content ($x = 0.2$) might be the maximum doping concentration of the respective elements that could be incorporated into the structure.

SEM images and EDS elemental maps of the pristine $\text{Eu}_{21}\text{Zn}_4\text{As}_{18}$ sample are shown in Figure 4. The backscattered image confirms the homogeneity and absence of a secondary phase, while the secondary electron image confirms the high density of the sample. The uniform distribution of each element is shown by the elemental maps. SEM images and elemental maps of Na-doped ($x = 0.1$) and K-doped ($x = 0.1$) samples are shown in SI, Figures S4 and S5. Compositional results of pristine $\text{Eu}_{21}\text{Zn}_4\text{As}_{18}$ and $\text{Eu}_{21-x}\text{K}_x\text{Zn}_4\text{As}_{18}$ ($x = 0.1$) samples from EDS are provided in the SI, Table S2. There are slight deviations from the nominal composition attributed to the close proximity of emission lines of the elements, as shown in SI, Figure S6. However, due to the large overlaps of Na K_α (1.04 keV) and Zn L_β (1.03 keV) emission lines, as shown in SI, Figure S7, the EDS compositional analysis of the $\text{Eu}_{21-x}\text{Na}_x\text{Zn}_4\text{As}_{18}$ ($x = 0.1$) sample is not provided. The density of the pressed pellets was >98% of the calculated density.

3.2. Magnetic Properties. Figure 5a shows the magnetic susceptibility vs temperature plot. At an applied field of 0.1 T, there is no difference between zero-field-cooled (ZFC) and field-cooled cooling (FCC) data. $\text{Eu}_{21}\text{Zn}_4\text{As}_{18}$ is paramagnetic at higher temperatures, consistent with the data previously reported for the antimony analog, $\text{Eu}_{21}\text{Zn}_4\text{Sb}_{18}$, by Suen et al.²⁴ The high-temperature paramagnetic behavior is expected for this compound containing Eu^{2+} with 7 unpaired core electrons in the 4f orbital. The Curie–Weiss law, $\chi(T) = C/(T - \theta)$, where χ is the magnetic susceptibility, C is the Curie constant, and θ is the Curie–Weiss temperature, is used to fit the portion of the data above the Neel temperature, $T_N = \sim 10$ K. It reveals an effective moment of $8.1 \mu_B$ per Eu, as shown in Figure 5b. This is slightly higher than, but close to, the theoretical value of the effective moment of free Eu^{2+} ions ($7.94 \mu_B$).²⁴ Europium compounds have exhibited an effective moment of $8.1 \mu_B$ per Eu due to the presence of divalent Eu cation previously.³⁴ Thus, the temperature-dependent magnetic susceptibility also confirms the Eu^{2+} content of the

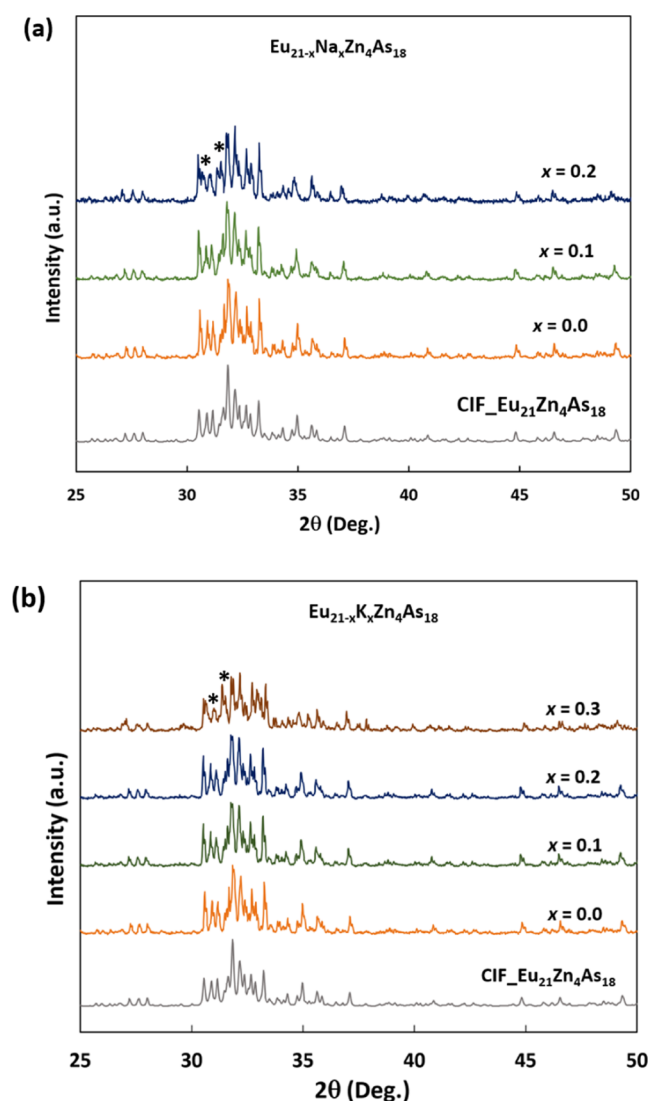


Figure 3. PXRD patterns of (a) $\text{Eu}_{21-x}\text{Na}_x\text{Zn}_4\text{As}_{18}$ ($x = 0.1, 0.2$) and (b) $\text{Eu}_{21-x}\text{K}_x\text{Zn}_4\text{As}_{18}$ ($x = 0.1, 0.2$). The PXRD patterns of pristine $\text{Eu}_{21}\text{Zn}_4\text{As}_{18}$ ($x = 0.0$) are added in both parts (a) and (b) as a reference for comparison purposes. Major impurity peaks are marked by asterisks (*).

compound. The magnetization shows a bend around 18 K and nearly remains constant around 10 K. Below 7 K, the magnetization starts to decrease, which resembles the behavior of antiferromagnetic ordering.

The positive Curie–Weiss temperature of 20.1 K indicates ferromagnetic interactions between Eu^{2+} , suggesting a more complex low-temperature magnetic ordering.²⁴ The field-dependent magnetization measurement at 2 K from 7 to -7 T is shown in Figure 5c. The magnetic moment starts to saturate around 3T. If all 21 Eu^{2+} ions were fully saturated, then the theoretical saturation moment would be $147 \mu_{\text{B}}$, which is slightly smaller than the experimentally determined saturated magnetic moment of $155.6 \mu_{\text{B}}$.

3.3. Thermal Transport Properties. Figure 6 represents the thermal transport properties of $\text{Eu}_{21}\text{Zn}_4\text{As}_{18}$ samples as a function of the temperature. The total thermal conductivity of the pristine $\text{Eu}_{21}\text{Zn}_4\text{As}_{18}$ sample is ultralow at $0.68 \text{ W m}^{-1} \text{ K}^{-1}$ at room temperature, owing to the complex crystal structure of the compound. It decreases to $0.42 \text{ W m}^{-1} \text{ K}^{-1}$ at 873 K. The

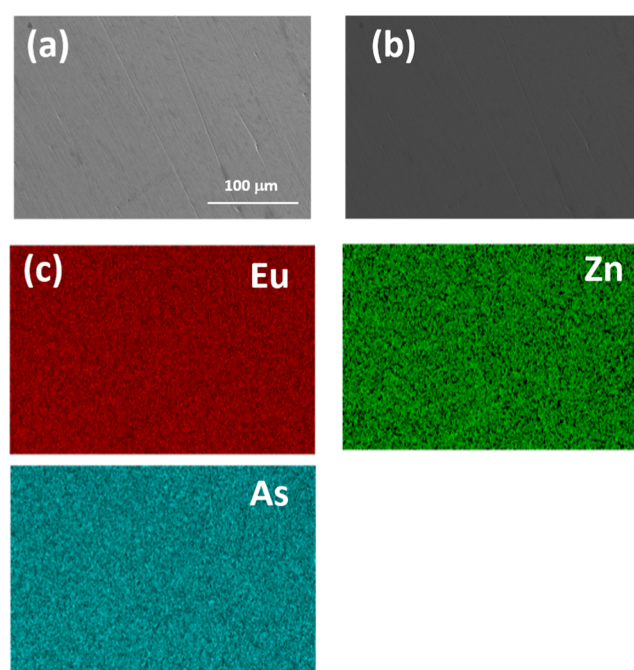


Figure 4. (a) Backscattered image of $\text{Eu}_{21}\text{Zn}_4\text{As}_{18}$ showing homogeneity of the compound. (b) Secondary electron image reveals the topography and high density of the pressed pellets. (c) Elemental maps from EDS show that Eu, Zn, and As are well-dispersed and homogeneously distributed in the compound.

decrease in total thermal conductivity with an increasing temperature is due to the Umklapp phonon–phonon scattering at high temperatures.

It is common to see extremely low lattice thermal conductivity in large complex crystal structures with many atoms. For instance, Zintl phases, such as $\text{Eu}_{11}\text{Zn}_4\text{Sn}_2\text{As}_{12}$,³⁵ Eu_2ZnSb_2 ,³⁶ $\text{Yb}_{14}\text{ZnSb}_{11}$,¹⁸ $\text{Yb}_{21}\text{Mn}_4\text{Sb}_{18}$,²⁶ and $\text{Yb}_{10}\text{MnSb}_9$,³⁷ have shown low total thermal conductivity dominated by lattice thermal conductivity with a very small contribution from electronic thermal conductivity. This is likely the case for $\text{Eu}_{21}\text{Zn}_4\text{As}_{18}$, potentially making this compound a good thermoelectric material. We calculated the lattice thermal conductivity of $\text{Eu}_{21}\text{Zn}_4\text{As}_{18}$ by subtracting the electronic portion of the thermal conductivity from the total thermal conductivity. The electronic thermal conductivity is estimated by the Wiedemann–Franz law, $\kappa_e = L\rho T$, where ρ is the electrical resistivity, T is the absolute temperature, and L is the Lorenz number (in $10^{-8} \text{ W } \Omega \text{ K}^2$). Assuming a parabolic band and acoustic phonon scattering, the simplified model of the Lorenz number is calculated by³⁸

$$L = 1.5 + \exp\left[-\frac{|S|}{116}\right]$$

where S is the Seebeck coefficient. The lattice thermal conductivity of pristine $\text{Eu}_{21}\text{Zn}_4\text{As}_{18}$ is $0.68 \text{ W m}^{-1} \text{ K}^{-1}$ at room temperature, which is indistinguishable from the total thermal conductivity due to the almost negligible contribution of the electronic thermal conductivity.

The total thermal conductivity of doped samples that have not shown any impurity phases is represented in SI, Figure S8. The Na- and K-doped samples show little to no changes in total thermal conductivity for the entire temperatures measured. There is a slight increase in the total thermal conductivity of the K-doped $\text{Eu}_{21-x}\text{K}_x\text{Zn}_4\text{As}_{18}$ ($x = 0.1$) sample

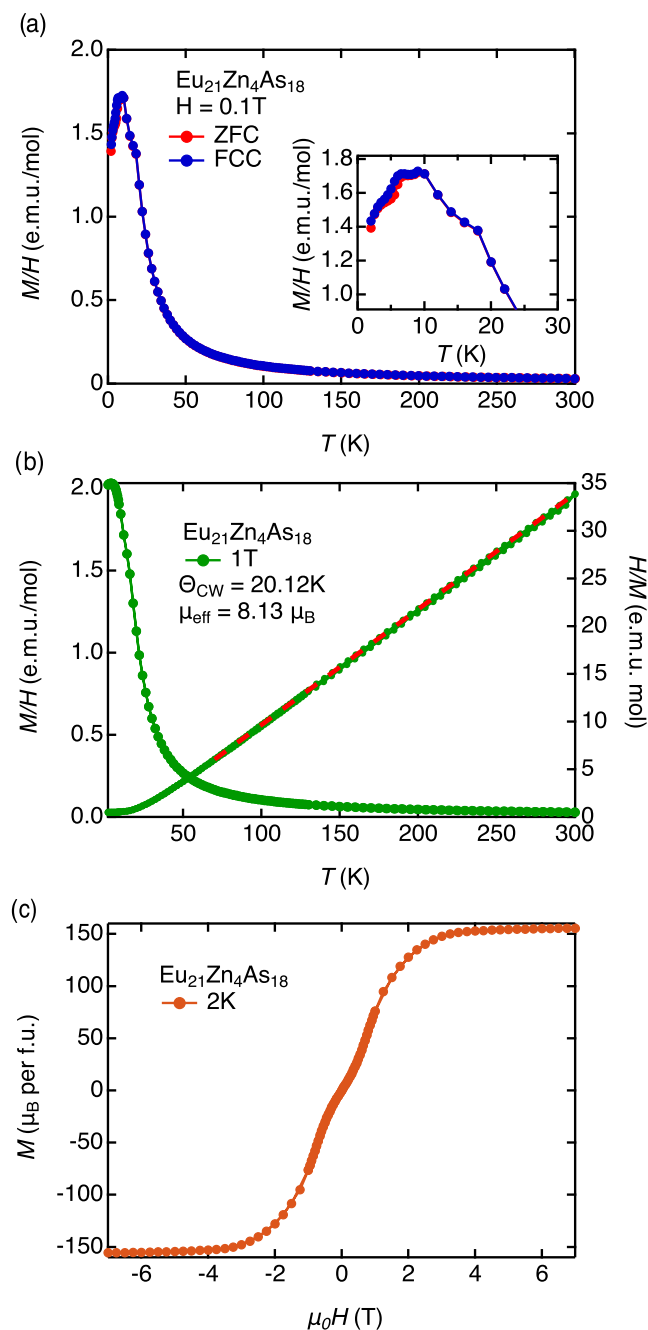


Figure 5. (a) Field-cooled cooling (FCC) and zero-field-cooled (ZFC) temperature-dependent magnetic susceptibility of pristine $\text{Eu}_{21}\text{Zn}_4\text{As}_{18}$ at 0.1 T. The inset shows the low-temperature magnetic phase transition. (b) Temperature-dependent magnetic susceptibility of $\text{Eu}_{21}\text{Zn}_4\text{As}_{18}$ at 1 T on the left-axis and H/M versus temperature with the Curie–Weiss fitting on the right axis. Red line represents the linear fit line. (c) Magnetization as a function of the magnetic field at 2 K. All markers are experimental data points.

compared with the pristine sample, which is within the error limit of the measurement. There is no significant effect of doping on the total thermal conductivity of $\text{Eu}_{21}\text{Zn}_4\text{As}_{18}$. Therefore, we focus our further analysis and discussion on the pristine ($x = 0.0$) sample.

3.4. Electronic Transport Properties. The temperature-dependent electronic transport properties of the pristine $\text{Eu}_{21}\text{Zn}_4\text{As}_{18}$ sample are shown in Figure 7. The pristine $\text{Eu}_{21}\text{Zn}_4\text{As}_{18}$ sample shows ultrahigh resistivity at low temper-

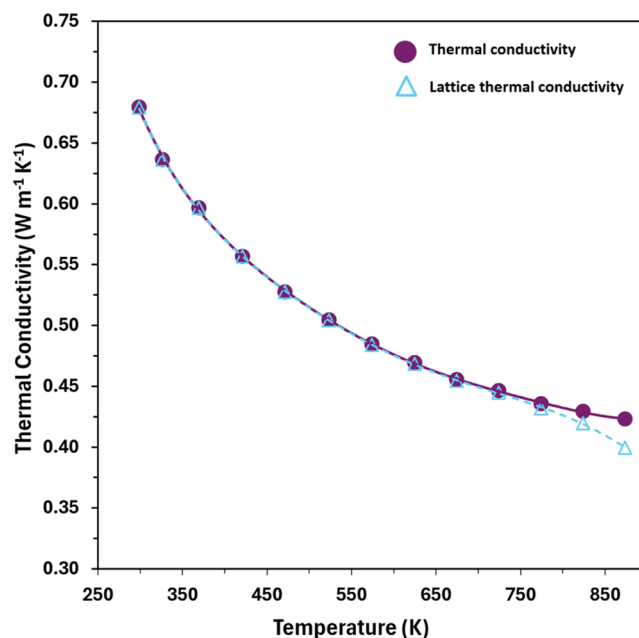


Figure 6. Temperature-dependent total thermal conductivity and lattice thermal conductivity of the $\text{Eu}_{21}\text{Zn}_4\text{As}_{18}$ sample. Markers are experimental data points.

atures. The resistivity starts at $29 \Omega \text{ cm}$ at 324 K and decreases to $0.53 \Omega \text{ cm}$ at 773 K, which is typical of a semiconductor.³⁹ Its resistivity is much higher than the only other 21-4-18 compound, $\text{Yb}_{21}\text{Mn}_4\text{Sb}_{18}$, reported until now for thermoelectric applications.²⁶ This unusually high resistivity implies the presence of very few intrinsic defects, which may be attributed to the strict stoichiometric control facilitated by the binary precursor-based synthesis of ternary Zintl phases.²⁷

The temperature-dependent Seebeck coefficient of $\text{Eu}_{21}\text{Zn}_4\text{As}_{18}$ is presented in Figure 7b. The Seebeck coefficients are positive over the entire temperature range measured, indicating the p-type transport properties. The Seebeck coefficient of the pristine sample increases from $444 \mu\text{V K}^{-1}$ at 321 K to a maximum of $545 \mu\text{V K}^{-1}$ at 446 K before decreasing. There is a sharp decline in the Seebeck coefficient in the temperature range of 500–780 K. This decline can be attributed to bipolar conduction, also indicated by the steep increase in Hall carrier concentration at the same temperature range. The overall efficiency of a thermoelectric material is limited by thermally excited minority carriers reaching the maximum Seebeck coefficient at a certain temperature.⁴⁰ This phenomenon is determined by the band gap of the compound. As a result, increasing the band gap could increase the thermopower of the compound, leading to better thermoelectric performance at higher temperatures. The Goldsmid–Sharp formula can be used to approximate the band gap from the maximum Seebeck coefficient and the corresponding temperature, $E_{\text{g}} = 2e|S|_{\text{max}}T_{\text{max}}$, where E_{g} is the band gap, $|S|_{\text{max}}$ is the maximum Seebeck coefficient, and T_{max} is the temperature of the maximum Seebeck coefficient.⁴¹ The band gap of $\text{Eu}_{21}\text{Zn}_4\text{As}_{18}$ is 0.49 eV, categorizing it as a narrow band gap semiconductor. The band gap is also estimated from the Arrhenius plot of electrical resistivity, yielding a value of 0.38 eV for pristine $\text{Eu}_{21}\text{Zn}_4\text{As}_{18}$, as shown in SI, Figure S9. So, the band gap of $\text{Eu}_{21}\text{Zn}_4\text{As}_{18}$ is larger than that of $\text{Eu}_{21}\text{Zn}_4\text{Sb}_{18}$ (0.2 eV), supporting our hypothesis that replacing antimony with arsenic would result in a higher band

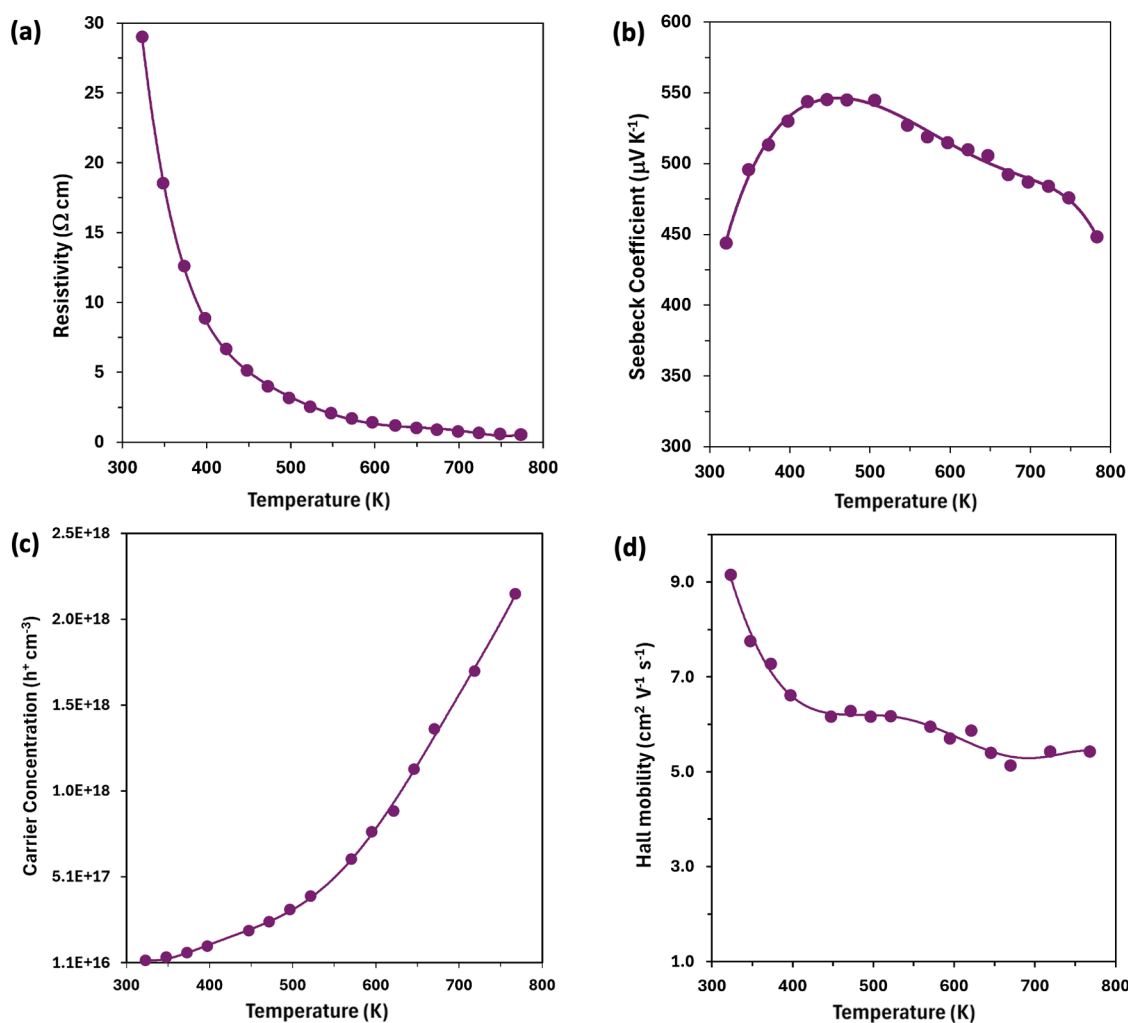


Figure 7. (a) Resistivity, (b) Seebeck coefficient, (c) Hall carrier concentration, and (d) Hall mobility of $\text{Eu}_{21}\text{Zn}_4\text{As}_{18}$ samples as a function of temperature. Markers are experimental data points.

gap in $\text{Eu}_{21}\text{Zn}_4\text{Pn}_{18}$ ($\text{Pn} = \text{As}, \text{Sb}$).^{24,42} Moreover, a high Seebeck coefficient might be attributed to a high effective mass, which is dependent on the overall density of state (DOS). Assuming a single parabolic band and acoustic phonon scattering to be the dominant scattering mechanism, the density of state effective mass of the pristine sample is calculated to be $m^* = 0.25 m_e$ at 373 K, $m^* = 0.54 m_e$ at 446 K, and $m^* = 0.73 m_e$ at 513 K. This evolution in the effective mass is likely due to the increasing Hall carrier concentration associated with charge carrier activation. Extrapolating the Seebeck coefficient to 0 K, it appears to linearly approach $0 \mu\text{V K}^{-1}$, in contrast to $\text{Yb}_{14}\text{MnSb}_{11}$.⁴³ With an effective dopant, we expect this effective mass to rise; presently, transport is limited to the very extrema of the valence band edge, and with a cell of this complexity, there are likely nearby lower energy bands.

The high resistivity in $\text{Eu}_{21}\text{Zn}_4\text{As}_{18}$ can also be explained by the temperature-dependent Hall carrier concentration data shown in Figure 7c. The positive values of the Hall coefficient indicate the p-type carrier transport of the compound. The Hall carrier concentration is $2.35 \times 10^{16} \text{ h}^+ \text{ cm}^{-3}$ at ~ 324 K for the pristine sample, which is much lower than that of heavily doped semiconductors considered ideal for thermoelectric applications.⁴⁴ The low carrier concentration could be attributed to the stoichiometric synthesis⁴⁵ and the Zintl bonding phenomena,⁴⁶ which assumes the complete transfer of

valence electrons from the cations to the anions. The low carrier concentration suggests a very low level of defects in this compound. Filled valence bands, where the valence bands and conduction bands do not overlap, lead to intrinsic semiconductor behavior, as exhibited by $\text{Eu}_{21}\text{Zn}_4\text{As}_{18}$, with a low charge carrier concentration.⁴⁷ The ultimate result is high resistivity in the compound because resistivity and carrier concentration are proportionally related by the following equation: $1/\rho = ne\mu$, where n is the Hall carrier concentration, e is the charge of an electron, and μ is the Hall mobility. Another avenue for further investigation could be tuning the carrier concentrations of the compound to $10^{20} \text{ h}^+ \text{ cm}^{-3}$ by doping the tetrahedron ZnAs_4 . For instance, $\text{Yb}_{21}\text{Mn}_4\text{Sb}_{18}$ was successfully doped with Cd^{2+} into the Mn^{2+} sites.²⁰ Despite the isoelectronic nature of the dopant, there was a considerable increase in hole carrier concentrations to $>10^{20} \text{ h}^+$ in doped $\text{Yb}_{21}\text{Mn}_{4-x}\text{Cd}_x\text{Sb}_{18}$ ($x = 1.5$), resulting in a zT of ~ 0.92 at 800 K due to more electronegative Cd providing more states for holes to occupy compared to Mn. However, the Seebeck coefficient is inversely related to the carrier concentration by the following equation, $S = (8\pi^2 k_B^2 / 3eh^2) m^* T (\pi/3n)^{2/3}$, where k_B is the Boltzmann's constant, e is the charge of an electron, h is the Planck's constant, m^* is the density of states effective mass, T is the temperature, and n is the carrier concentration. As a result, increasing the carrier concentration

will decrease the Seebeck coefficient, so systematically adjusting the carrier concentration is important.

The Hall carrier mobility of $\text{Eu}_{21}\text{Zn}_4\text{As}_{18}$ is illustrated in Figure 7d. $\text{Eu}_{21}\text{Zn}_4\text{As}_{18}$ shows a low Hall mobility of $9.14 \text{ cm}^2 \text{ V}^{-2} \text{ s}^{-1}$ at 324 K and decreases to $5.42 \text{ cm}^2 \text{ V}^{-2} \text{ s}^{-1}$ at 720 K. The mobility of the charge carrier decreases with increasing temperature for the pristine sample due to phonon scattering, a trend typically observed in semiconductors.⁴⁸ The presence of such low Hall carrier concentration and mobility can account for the ultrahigh resistivity of the pristine compound. This type of electronic transport behavior has been seen in a recently reported Zintl phase containing Eu, Zn, and As, the layered $\text{Eu}_{11}\text{Zn}_4\text{Sn}_2\text{As}_{18}$.³⁵

4. POWER FACTOR (PF) AND FIGURE OF MERIT

The power factor (PF) and the thermoelectric figure of merit zT as a function of temperature are presented in Figure 8a,b.

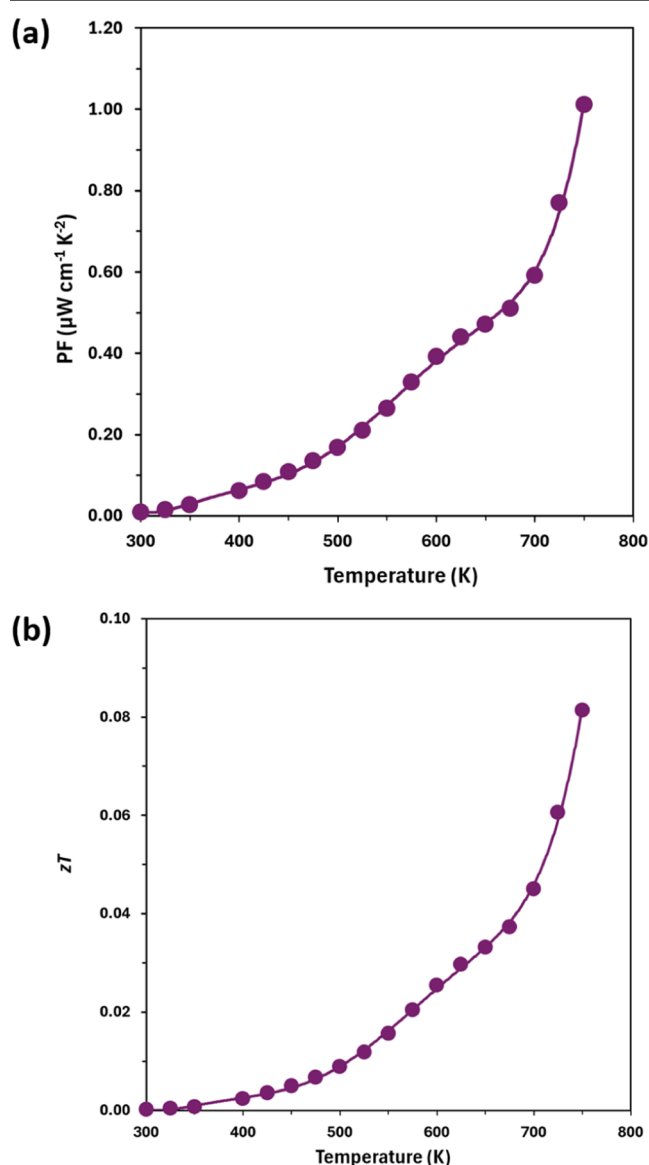


Figure 8. (a) Power factor and (b) thermoelectric figure of merit, zT as a function of the temperature of $\text{Eu}_{21}\text{Zn}_4\text{As}_{18}$. Calculated from polynomial fits to the temperature-dependent Seebeck coefficients, electrical resistivity, and thermal conductivity data.

The pristine $\text{Eu}_{21}\text{Zn}_4\text{As}_{18}$ sample shows a maximum zT of 0.08 at 750 K. This relatively low thermoelectric efficiency is primarily due to a low PF caused by significantly high resistivity. Thermal conductivity is close to the glassy limit, and further decreases are unlikely to be realized. Consequently, the electrical resistivity is this compound's main limiting factor in thermoelectric performance. Neither Na-doping nor K-doping into the Eu^{2+} sites has been an effective means of tuning the thermoelectric properties of the compound significantly. The thermoelectric properties of K-doped samples are presented in SI, Figure S10.

5. CONCLUSIONS

In summary, we present the thermoelectric properties of Zintl arsenide of 21-4-18 composition as a follow-up to our recently published article highlighting the limited availability of thermoelectric data on arsenic-based Zintl compounds.⁴⁹ We have shown that at the right temperature, binary precursors allow the synthesis of high-purity complex ternary-phase $\text{Eu}_{21}\text{Zn}_4\text{As}_{18}$ polycrystalline samples using the stoichiometric reaction of reagents. The magnetic properties measurement indicates paramagnetic behavior at high temperatures, consistent with that of other Eu^{2+} -containing compounds. The Curie–Weiss fit shows an effective moment of $7.94 \mu_{\text{B}}$, confirming the presence of only Eu^{2+} ions. Additionally, antiferromagnetic ordering has been observed at temperatures below 10 K. At 2 K, the magnetization measurement shows all 21 Eu^{2+} ions reaching saturation at 3T.

We measured the thermal and electronic transport properties of the compound to reveal its thermoelectric efficiency. This p-type narrow band gap semiconductor of $\sim 0.49 \text{ eV}$ boasts an ultralow thermal conductivity and a very high Seebeck coefficient, which are essential for achieving high thermoelectric efficiency. However, due to the high resistivity of pristine $\text{Eu}_{21}\text{Zn}_4\text{As}_{18}$, the overall thermoelectric efficiency, governed by the figure of merit zT , is low. This is attributed to the very low Hall carrier concentration ($\sim 10^{16} \text{ h}^+ \text{ cm}^{-3}$) of the pristine compound. In addition, the effect of cation site doping on the thermoelectric properties of the $\text{Eu}_{21}\text{Zn}_4\text{As}_{18}$ polycrystalline samples is studied. Neither Na^+ nor K^+ is shown to be an effective hole doping element at the present concentrations. Nonetheless, the unique structural properties, large volume, lattice thermal conductivity, and electronic band gap are attractive starting points, providing optimism for further research on this and other arsenic-containing 21-4-18 compositions.

■ ASSOCIATED CONTENT

Supporting Information

The Supporting Information is available free of charge at <https://pubs.acs.org/doi/10.1021/acs.chemmater.4c02200>.

Table of Rietveld refinement Parameters; table of EDS compositional analysis of pristine and K-doped samples; plots of X-ray powder diffraction patterns for binaries reagents; powder diffraction pattern of the reaction product synthesized at $1000 \text{ }^\circ\text{C}$ compared with possible phases; SEM backscattered images and elemental maps of Na- and K-doped samples; X-ray spectra of K-doped sample; temperature-dependent total thermal conductivity of all samples; Arrhenius plot for band gap from resistivity; resistivity, Seebeck, power factor, and zT for $\text{Eu}_{21-x}\text{K}_x\text{Zn}_4\text{As}_{18}$ ($x = 0.0, 0.1$) (PDF)

AUTHOR INFORMATION

Corresponding Author

Susan M. Kauzlarich – Department of Chemistry, University of California, Davis, California 95616, United States;

orcid.org/0000-0002-3627-237X;

Email: smkauzlarich@ucdavis.edu

Authors

Md. Minhajul Islam – Department of Chemistry, University of California, Davis, California 95616, United States;

orcid.org/0000-0002-6284-2946

Maria Wróblewska – Department of Physics, Colorado School of Mines, Golden, Colorado 80401, United States

Zihao Shen – Department of Physics and Astronomy, University of California, Davis, California 95616, United States

Eric S. Toberer – Department of Physics, Colorado School of Mines, Golden, Colorado 80401, United States

Valentin Taouf – Department of Physics and Astronomy, University of California, Davis, California 95616, United States

Complete contact information is available at:

<https://pubs.acs.org/10.1021/acs.chemmater.4c02200>

Notes

The authors declare no competing financial interest.

ACKNOWLEDGMENTS

This work was supported by the National Science Foundation, DMR-2307231. E.S.T. and M.W. acknowledge NSF DMR-2350519. Z.S. and V.T. acknowledge support from Peter Klavins and the UC Davis Physics Liquid Helium Laboratory Fund. The authors are grateful to the Advanced Materials Characterization and Testing Lab (AMCaT) in the UC Davis Department of Materials Science and Engineering for access to the SEM instrumentation. Part of this study was carried out at the UC Davis Center for Nano and Micro Manufacturing (CNM2).

REFERENCES

- (1) Pei, Y.; Shi, X.; LaLonde, A.; Wang, H.; Chen, L.; Snyder, G. J. Convergence of Electronic Bands for High Performance Bulk Thermoelectrics. *Nature* **2011**, *473* (7345), 66–69.
- (2) Deng, R.; Su, X.; Zheng, Z.; Liu, W.; Yan, Y.; Zhang, Q.; Dravid, V. P.; Uher, C.; Kanatzidis, M. G.; Tang, X. Thermal Conductivity in $\text{Bi}_{0.5}\text{Sb}_{1.5}\text{Te}_{3+x}$ and the Role of Dense Dislocation Arrays at Grain Boundaries. *Sci. Adv.* **2018**, *4* (6), No. eaar5606.
- (3) Biswas, K.; He, J.; Blum, I. D.; Wu, C.-I.; Hogan, T. P.; Seidman, D. N.; Dravid, V. P.; Kanatzidis, M. G. High-Performance Bulk Thermoelectrics with All-Scale Hierarchical Architectures. *Nature* **2012**, *489* (7416), 414–418.
- (4) Hsu, K. F.; Loo, S.; Guo, F.; Chen, W.; Dyck, J. S.; Uher, C.; Hogan, T.; Polychroniadis, E. K.; Kanatzidis, M. G. Cubic $\text{AgPb}_m\text{SbTe}_{2+m}$: Bulk Thermoelectric Materials with High Figure of Merit. *Science* **2004**, *303* (5659), 818–821.
- (5) Wu, H. J.; Zhao, L.-D.; Zheng, F. S.; Wu, D.; Pei, Y. L.; Tong, X.; Kanatzidis, M. G.; He, J. Q. Broad Temperature Plateau for Thermoelectric Figure of Merit $ZT > 2$ in Phase-Separated $\text{PbTe}_{0.7}\text{S}_{0.3}$. *Nat. Commun.* **2014**, *5* (1), No. 4515.
- (6) Xiao, Y.; Wang, D.; Zhang, Y.; Chen, C.; Zhang, S.; Wang, K.; Wang, G.; Pennycook, S. J.; Snyder, G. J.; Wu, H.; Zhao, L.-D. Band Sharpening and Band Alignment Enable High Quality Factor to Enhance Thermoelectric Performance in n -Type PbS . *J. Am. Chem. Soc.* **2020**, *142* (8), 4051–4060.
- (7) Kauzlarich, S. M.; Brown, S. R.; Jeffrey Snyder, G. Zintl Phases for Thermoelectric Devices. *Dalton Trans.* **2007**, No. 21, 2099.
- (8) Boyko, M.; Hlukhyy, V.; Fässler, T. F. $\text{K}_7\text{In}_4\text{As}_6$ and K_3InAs_2 - Two More Zintl Phases Showing the Rich Variety of In-As Polyanion Structures. *Z. Anorg. Allg. Chem.* **2023**, *649* (21), No. e202300164.
- (9) Baranets, S.; Darone, G. M.; Bobev, S. Synthesis and Structure of $\text{Sr}_{14}\text{Zn}_{1+x}\text{As}_{11}$ and $\text{Eu}_{14}\text{Zn}_{1+x}\text{As}_{11}$ ($x \leq 0.5$). New Members of the Family of Pnictides Isotypic with $\text{Ca}_{14}\text{AlSb}_{11}$, Exhibiting a New Type of Structural Disorder. *J. Solid State Chem.* **2019**, *280*, No. 120990.
- (10) Baranets, S.; Kandabadi, T.; Wang, X.; Bai, X.; Young, D. P.; Bobev, S. Quaternary Zintl Phases $\text{Ba}_2\text{InSnP}_3$ and $\text{Ba}_2\text{InSnAs}_3$ with Complex Structures and n -Type Semiconducting Behavior. *Chem. Mater.* **2024**, *36* (15), 7570–7580.
- (11) Ishtiyak, M.; Watts, S. R.; Thiye, B.; Womack, F.; Adams, P.; Bai, X.; Young, D. P.; Bobev, S.; Baranets, S. Advancing Heteroanionicity in Zintl Phases: Crystal Structures, Thermoelectric and Magnetic Properties of Two Quaternary Semiconducting Arsenide Oxides, $\text{Eu}_8\text{Zn}_2\text{As}_6\text{O}$ and $\text{Eu}_{14}\text{Zn}_5\text{As}_{12}\text{O}$. *Inorg. Chem.* **2024**, *63*, 20226–20239.
- (12) Ono, K.; Kihou, K.; Usui, H.; Kuroki, K.; Goto, Y.; Lee, C.-H. $\text{Rb}(\text{Zn,Cu})_4\text{As}_3$ as a New High-Efficiency Thermoelectric Material. *ACS Omega* **2023**, *8* (45), 42900–42906.
- (13) Ogunbunmi, M. O.; Baranets, S.; Childs, A. B.; Bobev, S. The Zintl Phases AlnAs_2 ($A = \text{Ca, Sr, Ba}$): New Topological Insulators and Thermoelectric Material Candidates. *Dalton Trans.* **2021**, *50* (26), 9173–9184.
- (14) Cao, W.; Wu, J.; Li, Y.; Pei, C.; Wang, Q.; Zhao, Y.; Li, C.; Zhu, S.; Zhang, M.; Zhang, L.; Chen, Y.; Wang, Z.; Qi, Y. Pressure-Induced Superconductivity and Structure Phase Transition in SnAs -Based Zintl Compound SrSn_2As_2 . *Adv. Phys. Res.* **2024**, *3* (6), No. 2300149.
- (15) Harmer, C. P.; Pak, C.; Greenfield, J. T.; Adeyemi, A. N.; Gamage, E. H.; Kovnir, K. Non-Innocent Intercalation of Diamines into Tetragonal FeS Superconductor. *ACS Appl. Energy Mater.* **2021**, *4* (1), 42–46.
- (16) Jo, N. H.; Kuthanazhi, B.; Wu, Y.; Timmons, E.; Kim, T.-H.; Zhou, L.; Wang, L.-L.; Ueland, B. G.; Palasyuk, A.; Ryan, D. H.; McQueeney, R. J.; Lee, K.; Schrunck, B.; Burkov, A. A.; Prozorov, R.; Bud'ko, S. L.; Kaminski, A.; Canfield, P. C. Manipulating Magnetism in the Topological Semimetal EuCd_2As_2 . *Phys. Rev. B* **2020**, *101* (14), No. 140402.
- (17) Jana, M. K.; Biswas, K. Crystalline Solids with Intrinsically Low Lattice Thermal Conductivity for Thermoelectric Energy Conversion. *ACS Energy Lett.* **2018**, *3* (6), 1315–1324.
- (18) Justl, A. P.; Ricci, F.; Pike, A.; Cerretti, G.; Bux, S. K.; Hautier, G.; Kauzlarich, S. M. Unlocking the Thermoelectric Potential of the $\text{Ca}_{14}\text{AlSb}_{11}$ Structure Type. *Sci. Adv.* **2022**, *8* (36), No. eabq3780.
- (19) Borgsmiller, L.; Li, Q.; Toriyama, M. Y.; Snyder, G. J. New Zintl Phase $\text{Yb}_{10}\text{MgSb}_9$ with High Thermoelectric Performance. *Adv. Energy Mater.* **2023**, *13* (19), No. 2300393.
- (20) He, A.; Cerretti, G.; Kauzlarich, S. M. The Impact of Site Selectivity and Disorder on the Thermoelectric Properties of $\text{Yb}_{21}\text{Mn}_4\text{Sb}_{18}$ Solid Solutions: $\text{Yb}_{21}\text{Mn}_{4-x}\text{Cd}_x\text{Sb}_{18}$ and $\text{Yb}_{21-y}\text{Ca}_y\text{Mn}_4\text{Sb}_{18}$. *Mater. Adv.* **2021**, *2* (17), 5764–5776.
- (21) Toberer, E. S.; Zevalkink, A.; Snyder, G. J. Phonon Engineering through Crystal Chemistry. *J. Mater. Chem.* **2011**, *21* (40), 15843.
- (22) Kauzlarich, S. M.; Zevalkink, A.; Toberer, E.; Snyder, G. J. Zintl Phases: Recent Developments in Thermoelectrics and Future Outlook. In *Thermoelectric Materials and Devices*; Nandhakumar, I., White, N. M., Beeby, S., Eds.; Royal Society of Chemistry, 2016; pp 1–26. DOI: 10.1039/9781782624042-00001.
- (23) Xia, S.-Q.; Bobev, S. Zintl Phase Variations Through Cation Selection. Synthesis and Structure of $\text{A}_2\text{Cd}_4\text{Pn}_{18}$ ($A = \text{Eu, Sr, Ba; Pn} = \text{Sb, Bi}$). *Inorg. Chem.* **2008**, *47* (6), 1919–1921.
- (24) Suen, N.-T.; Wang, Y.; Bobev, S. Synthesis, Crystal Structures, and Physical Properties of the New Zintl Phases $\text{A}_2\text{Zn}_4\text{Pn}_{18}$ ($A = \text{Ca, Eu; Pn} = \text{As, Sb}$)—Versatile Arrangements of $[\text{ZnPn}_4]$ Tetrahedra. *J. Solid State Chem.* **2015**, *227*, 204–211.

- (25) Xia, S.-q.; Bobev, S. Diverse Polyanions Based on MnBi_4 and MnSb_4 Tetrahedra: Polymorphism, Structure, and Bonding in $\text{Ca}_{21}\text{Mn}_4\text{Bi}_{18}$ and $\text{Ca}_{21}\text{Mn}_4\text{Sb}_{18}$. *Inorg. Chem.* **2007**, *46* (3), 874–883.
- (26) He, A.; Bux, S. K.; Hu, Y.; Uhl, D.; Li, L.; Donadio, D.; Kauzlarich, S. M. Structural Complexity and High Thermoelectric Performance of the Zintl Phase: $\text{Yb}_{21}\text{Mn}_4\text{Sb}_{18}$. *Chem. Mater.* **2019**, *31* (19), 8076–8086.
- (27) Justl, A. P.; Cerretti, G.; Bux, S. K.; Kauzlarich, S. M. $2 + 2 = 3$: Making Ternary Phases through a Binary Approach. *Chem. Mater.* **2022**, *34* (3), 1342–1355.
- (28) Toby, B. H.; Von Dreele, R. B. *GSAS-II: The Genesis of a Modern Open-Source All Purpose Crystallography Software Package*. *J. Appl. Crystallogr.* **2013**, *46* (2), 544–549.
- (29) Iwanaga, S.; Toberer, E. S.; LaLonde, A.; Snyder, G. J. A High Temperature Apparatus for Measurement of the Seebeck Coefficient. *Rev. Sci. Instrum.* **2011**, *82* (6), No. 063905.
- (30) Borup, K. A.; Toberer, E. S.; Zoltan, L. D.; Nakatsukasa, G.; Errico, M.; Fleurial, J.-P.; Iversen, B. B.; Snyder, G. J. Measurement of the Electrical Resistivity and Hall Coefficient at High Temperatures. *Rev. Sci. Instrum.* **2012**, *83* (12), No. 123902.
- (31) Kim, H.; Condon, C. L.; Holm, A. P.; Kauzlarich, S. M. Synthesis, Structure, and Magnetic Properties of a New Ternary Zintl Phase: $\text{Sr}_{21}\text{Mn}_4\text{Sb}_{18}$. *J. Am. Chem. Soc.* **2000**, *122* (43), 10720–10721.
- (32) Cordova, D. L. M.; Johnson, D. C. Synthesis of Metastable Inorganic Solids with Extended Structures. *ChemPhysChem* **2020**, *21* (13), 1345–1368.
- (33) Rietveld, H. M. A Profile Refinement Method for Nuclear and Magnetic Structures. *J. Appl. Crystallogr.* **1969**, *2* (2), 65–71.
- (34) Stavinoha, M.; Huang, C.-L.; Devlin, K. P.; Fettinger, J. C.; Kauzlarich, S. M.; Morosan, E. Size, Disorder, and Charge Doping Effects in the Antiferromagnetic Series $\text{Eu}_{1-x}\text{A}_x\text{Ga}_4$ ($\text{A} = \text{Ca}, \text{Sr}, \text{or La}$). *J. Solid State Chem.* **2020**, *285*, No. 121232.
- (35) Hauble, A. K.; Toriyama, M. Y.; Bartling, S.; Abdel-Mageed, A. M.; Snyder, G. J.; Kauzlarich, S. M. Experiment and Theory in Concert To Unravel the Remarkable Electronic Properties of Na-Doped $\text{Eu}_{11}\text{Zn}_4\text{Sn}_2\text{As}_{12}$: A Layered Zintl Phase. *Chem. Mater.* **2023**, *35* (18), 7719–7729.
- (36) Chen, C.; Xue, W.; Li, S.; Zhang, Z.; Li, X.; Wang, X.; Liu, Y.; Sui, J.; Liu, X.; Cao, F.; Ren, Z.; Chu, C.-W.; Wang, Y.; Zhang, Q. Zintl-Phase Eu_2ZnSb_2 : A Promising Thermoelectric Material with Ultralow Thermal Conductivity. *Proc. Natl. Acad. Sci. U.S.A.* **2019**, *116* (8), 2831–2836.
- (37) Borgsmiller, L.; Snyder, G. J. Thermoelectric Properties and Low Thermal Conductivity of Zintl Compound $\text{Yb}_{10}\text{MnSb}_9$. *J. Mater. Chem. A* **2022**, *10* (28), 15127–15135.
- (38) Kim, H.-S.; Gibbs, Z. M.; Tang, Y.; Wang, H.; Snyder, G. J. Characterization of Lorenz Number with Seebeck Coefficient Measurement. *APL Mater.* **2015**, *3* (4), No. 041506.
- (39) Seeger, K. *Elementary Properties of Semiconductors*. In *Semiconductor Physics*; Advanced Texts in Physics; Springer: Berlin, 2004; pp 1–9.
- (40) Pei, Y.; Wang, H.; Snyder, G. J. Band Engineering of Thermoelectric Materials. *Adv. Mater.* **2012**, *24* (46), 6125–6135.
- (41) Goldsmid, H. J.; Sharp, J. W. Estimation of the Thermal Band Gap of a Semiconductor from Seebeck Measurements. *J. Electron. Mater.* **1999**, *28* (7), 869–872.
- (42) Soheilnia, N.; Xu, H.; Zhang, H.; Tritt, T. M.; Swainson, I.; Kleinke, H. Thermoelectric Properties of $\text{Re}_3\text{Ge}_{0.6}\text{As}_{6.4}$ and Re_3GeAs_6 in Comparison to $\text{Mo}_3\text{Sb}_{5.4}\text{Te}_{1.6}$. *Chem. Mater.* **2007**, *19* (16), 4063–4068.
- (43) Toberer, E. S.; Cox, C. A.; Brown, S. R.; Ikeda, T.; May, A. F.; Kauzlarich, S. M.; Snyder, G. J. Traversing the Metal-Insulator Transition in a Zintl Phase: Rational Enhancement of Thermoelectric Efficiency in $\text{Yb}_{14}\text{Mn}_{1-x}\text{Al}_x\text{Sb}_{11}$. *Adv. Funct. Mater.* **2008**, *18* (18), 2795–2800.
- (44) Markov, M.; Rezaei, S. E.; Sadeghi, S. N.; Esfarjani, K.; Zebajadi, M. Thermoelectric Properties of Semimetals. *Phys. Rev. Mater.* **2019**, *3* (9), No. 095401.
- (45) Zevalkink, A.; Takagiwa, Y.; Kitahara, K.; Kimura, K.; Snyder, G. J. Thermoelectric Properties and Electronic Structure of the Zintl Phase $\text{Sr}_3\text{Al}_2\text{Sb}_6$. *Dalton Trans.* **2014**, *43* (12), 4720.
- (46) Pomrehn, G. S.; Zevalkink, A.; Zeier, W. G.; van de Walle, A.; Snyder, G. J. Defect-Controlled Electronic Properties in AZn_2Sb_2 Zintl Phases. *Angew. Chem., Int. Ed.* **2014**, *53* (13), 3422–3426.
- (47) Nesper, R. Structure and Chemical Bonding in Zintl-Phases Containing Lithium. *Prog. Solid State Chem.* **1990**, *20* (1), 1–45.
- (48) Yu, P. Y.; Cardona, M. Electrical Transport. In *Fundamentals of Semiconductors*; Graduate Texts in Physics; Springer: Berlin, 2010; pp 203–241.
- (49) Islam, Md. M.; Kauzlarich, S. M. The Potential of Arsenic-based Zintl Phases as Thermoelectric Materials: Structure & Thermoelectric Properties. *Z. Anorg. Allg. Chem.* **2023**, *649* (21), No. e202300149.